International Symposium
On Turbulence and Shear Flow
Phenomena (TSFP-8)
August 28 - 30, 2013 Poitiers, France

WALL PRESSURE FLUCTUATIONS INDUCED BY COHERENT STRUCTURES IN TURBULENT PIPE FLOW

M Luhar
Graduate Aerospace Laboratories
California Institute of Technology
Pasadena, CA 91125, USA
mluhar@caltech.edu

A S Sharma
Engineering and the Environment
University of Southampton
Highfield, Southampton, SO17 1BJ, UK
a.sharma@soton.ac.uk

B J McKeon
Graduate Aerospace Laboratories
California Institute of Technology
Pasadena, CA 91125, USA
mckeon@caltech.edu

ABSTRACT

We extend the simple forcing-response model developed by McKeon & Sharma (2010) to predict the wall pressure field associated with coherent structures in turbulent pipe flow. Realistic coherent structures such as modulating packets of hairpin vortices arise from the superposition of a small number of the velocity response modes predicted by this model. The wall pressure fluctuations associated with these velocity response modes capture many features observed in laboratory experiments and DNS, such as the location of pressure minima beneath coherent structures, the near-circular aspect ratio of wall pressure fluctuations, and the discrepancy in the characteristic length scales associated with the streamwise velocity and wall pressure fluctuations.

INTRODUCTION

The fluctuating wall pressure induced by turbulent flows is important across a range of engineering problems - from aerodynamic noise generation and structural loading, to sediment transport in river channels. Further, the wall pressure field is coupled to turbulent velocity fluctuations across the entire domain via a Poisson equation (Kim, 1989), and the wall-parallel gradient of wall pressure is directly proportional to the flux of vorticity from the wall (Koumoutsakos, 1999). As a result, an improved understanding of the wall pressure field could also benefit flow diagnostics and control.

Unfortunately, there are many technical challenges associated with obtaining accurate wall pressure measurements. The small spatial scales associated with turbulent flows impose severe sensor size limitations (Schewe, 1983; Klewicki *et al.*, 2008). The presence of significant background noise and structural vibration results in inherently noisy measurements that require careful correction (Tsuji *et al.*, 2007, 2012). Recent advances in Direct Numerical Simulation (DNS) (Jimenez & Hoyas, 2008), along with improved pressure measurement techniques and the development of large-scale, high Reynolds number flow facilities (Tsuji *et al.*, 2007; Klewicki *et al.*, 2008) have provided significant insight into the statistical nature of the wall pressure field. Some well-established theoretical predictions, such as the presence of a k^{-1} spectral range (k is the streamwise wavenumber), as well as the logarithmic increase of inner normalized mean-square wall pressure $\left(p_w'^2\right)^+$ with Reynolds number have been confirmed (Jimenez & Hoyas, 2008; Klewicki *et al.*, 2008). (Note: throughout this paper, a superscript $+$ refers to normalization with respect to the friction velocity, u_τ, and kinematic viscosity, ν.)

Despite these advances, the structural nature and origin of the wall pressure field is less well established. This is because an accurate structural description requires temporally- and spatially-resolved wall pressure data. The resulting storage and processing requirements compound any technical challenges associated with obtaining such data in the first place. Broadly, numerical (Kim, 1989; Jimenez & Hoyas, 2008) and experimental (Klewicki *et al.*, 2008) results agree that, unlike the streamwise velocity fluctuations, wall pressure fluctuations are nearly circular in terms of aspect ratio (i.e., comparable streamwise and spanwise length scales). Yet, there is little consensus on the characteristic length scales and advection speeds associated with the wall pressure field.

In this paper, we use the forcing-response model developed by McKeon & Sharma (2010) to study the wall pressure field associated with the passage of coherent structures in turbulent pipe flow. Although we only consider pipe flow, we expect our results to be applicable across different flow configurations (e.g. channel and boundary-layer flow). The model employs the Navier-Stokes equations (NSE), Fourier-transformed in the homogeneous spatial directions and in time, along with an assumed mean velocity profile. Under the Fourier transform, each wavenumber-frequency combination corresponds to an obliquely propagating wave. The nonlinear advective terms in the NSE are treated as an unstructured forcing. The well-known linear Navier-Stokes resolvent operator maps this nonlinear forcing to a velocity response. Note that the mean velocity is sustained in the full model but is assumed here for convenience. With

this assumption, the system can be considered as a series of linear sub-units (corresponding to each wavenumber-frequency combination) with unstructured forcing. A singular value decomposition of the resolvent operator identifies the highest-gain forcing and response mode shapes (i.e., profiles in the inhomogeneous wall-normal direction). McKeon & Sharma (2010) show that, in general, the velocity response modes identified by this model resemble the near singular critical-layer solutions obtained via classical, linear Orr-Sommerfeld-Squire analyses. Further, the response modes appear consistent with observations in real flows.

More recently, Sharma & McKeon (2013) have shown that structures resembling hairpin vortices arise naturally from the superposition of a pair of obliquely propagating critical-layer velocity response modes, with spanwise wavenumber $\pm n$. More complex structures, such as modulating packets of hairpin vortices, arise from the superposition of three obliquely propagating mode pairs ($\pm n$) that are triadically consistent in terms of frequency and wavenumber. In what follows, we study the wall pressure field associated with such model structures. We show that these simple models are able to qualitatively reproduce many of the observed structural features of the wall pressure field beneath wall turbulence.

FORCING-RESPONSE MODEL (RESOLVENT ANALYSIS)

This section provides a brief review of the model developed by McKeon & Sharma (2010), and describes the extension to include pressure. We consider turbulent flow through a long cylindrical pipe. Given the statistical homogeneity in the streamwise direction and in time, along with the integer constraint on azimuthal (spanwise) wavenumber, the total turbulent velocity field, $\tilde{\mathbf{u}}$, can be expressed as a superposition of Fourier modes with streamwise wavenumber k, spanwise wavenumber n, and temporal frequency, ω:

$$\tilde{\mathbf{u}}(x,y,\theta,t) = \sum_n \int_{-\infty}^{\infty}\int_{-\infty}^{\infty} \mathbf{u}_{\mathbf{k}}(y) e^{i(kx+n\theta-\omega t)} dk\, d\omega \quad (1)$$

Here, x and θ are the streamwise and azimuthal directions, respectively, and t is time. The wall-normal coordinate is $y = 1-r$, where r is the radial coordinate normalized by pipe radius, R. Retaining boundary-layer terminology, the velocity vector $\tilde{\mathbf{u}} = (\tilde{u},\tilde{v},\tilde{w})$ represents the streamwise ($\tilde{u}$), wall-normal ($\tilde{v}$), and azimuthal velocities ($\tilde{w}$). The turbulent mean velocity profile is $\mathbf{u_0} = (U(y),0,0)$, and the fluctuating velocity field is $\mathbf{u} = \tilde{\mathbf{u}} - \mathbf{u_0}$. At each wavenumber-frequency combination, $\mathbf{k} = (k,n,\omega)$, this Fourier decomposition yields an input-output relationship. The nonlinear advective terms in the NSE are treated as an unstructured forcing (input) to the system, $\mathbf{f_k} = (\mathbf{u}\cdot\nabla\mathbf{u})_\mathbf{k}$. The Navier-Stokes resolvent operator, $\mathscr{H}_\mathbf{k}$, comprises the transfer functions that map this forcing to the velocity response (output).

McKeon & Sharma (2010) projected the NSE onto a space of divergence-free basis functions that satisfied the correct boundary conditions, $\mathbf{u_k}(y=0)=0$, to eliminate the pressure term and satisfy mass continuity. To capture the fluctuating pressure associated with the velocity response modes, the forcing-response system is derived directly in terms of the so-called *primitive* variables instead. Pressure, $p_\mathbf{k}$, is retained explicitly in the formulation:

$$\begin{bmatrix}\mathbf{u_k}(y)\\ p_\mathbf{k}(y)\end{bmatrix} = \left(-i\omega\begin{bmatrix}\mathbf{I} & \\ & 0\end{bmatrix} - \begin{bmatrix}\mathscr{L}_\mathbf{k} & -\nabla_\mathbf{k}\\ \nabla_\mathbf{k}^T & 0\end{bmatrix}\right)^{-1}\begin{bmatrix}\mathbf{I} & \\ & 0\end{bmatrix}\mathbf{f_k}$$

$$= \mathscr{H}_\mathbf{k}(y)\mathbf{f_k}(y) \quad (2)$$

Here, $\mathscr{H}_\mathbf{k}$ is a modified resolvent operator, $\mathscr{L}_\mathbf{k}(\mathbf{k},\mathbf{u_0},Re)$ is the linear Navier-Stokes operator and Re is the Reynolds number. The first row of the operator inside the parentheses on the right-hand side of (2) represents the momentum equations, while the last row represents continuity. Following McKeon & Sharma (2010), a singular value decomposition of the discretized resolvent operator,

$$\mathscr{H}_\mathbf{k} = \sum_m \mathbf{u}_{\mathbf{k},m}\sigma_m\mathbf{f}^*_{\mathbf{k},m}$$

with

$$\sigma_1 > \sigma_2 \ldots > \sigma_m > 0 \quad (3)$$
$$\mathbf{f}^*_{\mathbf{k},l}\mathbf{f}_{\mathbf{k},m} = \delta_{lm}$$
$$\mathbf{u}^*_{\mathbf{k},l}\mathbf{u}_{\mathbf{k},m} = \delta_{lm}$$

identifies the forcing mode shape $\mathbf{f}_{\mathbf{k},1}(y)$ that leads to the most *amplified* velocity response $\sigma_{\mathbf{k},1}\mathbf{u}_{\mathbf{k},1}(y)$ under an L^2 (energy) norm. A superscript (*) denotes the conjugate transpose.

McKeon & Sharma (2010) show that large velocity responses (high $\sigma_{\mathbf{k},1}$) arise through two mechanisms: via the lift-up mechanism associated with the high mean shear close to the wall, or at the critical layer where the phase speed of the propagating mode matches the local mean velocity, $c = \omega/k = U$. As mentioned earlier, in the latter case, the velocity response modes closely resemble the critical-layer solutions obtained from classical linear Orr-Sommerfeld-Squire analyses. Extending the concepts of linear stability analysis to the present turbulent case, the first singular response modes $\mathbf{u}_{\mathbf{k},1}$ are, in a sense, the *least damped* velocity fields. They are sustained by minimal forcing in the direction of $\mathbf{f}_{\mathbf{k},1}$. The importance of linear processes in turbulent wall flows has been recognized for some time (Kim, 2003). The model considered here identifies the nonlinear interactions as a forcing to the linear system.

Importantly, analysis of the resolvent operator at $\mathbf{k}$ combinations observed in real turbulence suggests that these transfer functions are effectively low-rank. Only, a limited number of input directions, $\mathbf{f}_{\mathbf{k},m}$ are highly amplified and so the velocity field $\mathbf{u_k}$ may be reasonably approximated by the first singular response, $\mathbf{u}_{\mathbf{k},1}$. In other words, the first singular response mode is so highly amplified that it dominates the velocity field, as long as a non-zero component of forcing exists along $\mathbf{f}_{\mathbf{k},1}$ in the real flow. Recent studies by Sharma & McKeon (2013) and Moarref *et al.* (2013) have shown that this low-rank model captures many of the key statistical and structural properties of wall turbulence. As a result, we consider only the first singular forcing and response modes for the remainder of this paper. For notational convenience, we drop the additional subscript 1.

PRESSURE POISSON EQUATION

Taking the divergence of the momentum equation (top line of 2) yields the Poisson equation for the turbulent pressure field in incompressible flows. The source terms in the

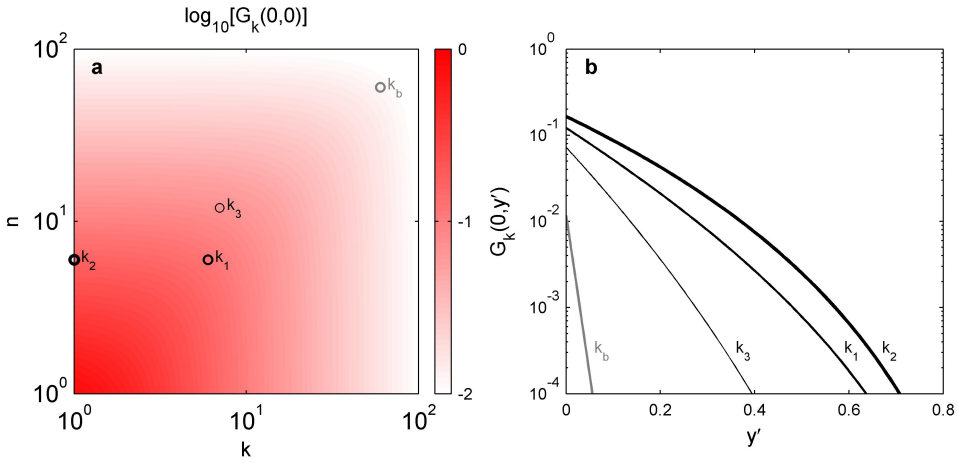

Figure 1: (a) Log-spaced contours showing the magnitude of the Green's function at the wall for source terms at the wall. (b) Green's functions for wall pressure for the four wavenumber combinations marked in (a), $\mathbf{k}_1 = (6,6)$ (black line), $\mathbf{k}_2 = (1,6)$ (bold black line), $\mathbf{k}_3 = (7,12)$ (fine black line), and $\mathbf{k}_b = (60,60)$ (gray line).

pressure Poisson equation consist of a linear or *rapid* contribution arising from the product of the mean shear (U') and streamwise gradient of wall-normal velocity ($ikv_{\mathbf{k}}$), and a nonlinear or *slow* contribution representing interactions between the fluctuating velocity components ($\nabla_{\mathbf{k}} \cdot \mathbf{f}_{\mathbf{k}}$):

$$\nabla^2_{\mathbf{k}} p_{\mathbf{k}} = -2ikv_{\mathbf{k}}U' + \nabla_{\mathbf{k}} \cdot \mathbf{f}_{\mathbf{k}} \tag{4}$$

The DNS of Kim (1989) and Jimenez & Hoyas (2008) suggest that the slow component of pressure is dominant except very close to the wall. Near the wall, the rapid component of pressure tends to be larger. However, in general, the magnitude of both terms is comparable. The resolvent analysis approach considered here emphasizes linear mechanisms. Hence, we expect our model to yield reasonable predictions for the rapid component of pressure associated with each mode. The slow component of pressure depends on nonlinear interactions, requiring additional knowledge about the relative magnitude and phase of each mode.

The fluctuating pressure field must satisfy the following Neumann boundary condition at the wall, which results from the wall-normal momentum equation:

$$\frac{\partial p_{\mathbf{k}}}{\partial r}(r=1) = \frac{1}{Re}\left[\frac{1}{r}\frac{\partial}{\partial r}\left(r\frac{\partial v_{\mathbf{k}}}{\partial r}\right)\right] \tag{5}$$

However, previous studies (Kim, 1989) show that the effect of this inhomogeneous boundary condition is negligible at high Reynolds number and that it may be replaced by

$$\frac{\partial p_{\mathbf{k}}}{\partial r}(r=1) = 0 \tag{6}$$

Although the inhomogeneous wall boundary condition (5) does not significantly affect the pressure field, this does not imply that the presence of the wall does not significantly affect pressure fluctuations. Kim (1989) suggests that the effect of the wall is built into the source terms in (4), via the no-slip boundary condition instead.

Green's Function Solution

To gain further insight into the nature of the fluctuating wall pressure associated with the velocity response modes at each $\mathbf{k}$, we consider a Green's function representation. It can be shown that the Green's function for (4) and (6) corresponding to $(k,n) \neq 0$ is:

$$G_{\mathbf{k}}(r,r') = \begin{cases} -A_{\mathbf{k}} I_n(kr') I_n(kr) - I_n(kr') K_n(kr), & r > r' \\ -A_{\mathbf{k}} I_n(kr') I_n(kr) - I_n(kr) K_n(kr'), & r < r' \end{cases} \tag{7}$$

with

$$A_{\mathbf{k}} = \frac{K_{n-1}(k) + K_{n+1}(k)}{I_{n-1}(k) + I_{n+1}(k)} \tag{8}$$

Here, I_n and K_n are modified Bessel functions. Using (7), the solution to (4) becomes:

$$p_{\mathbf{k}}(r) = \int_0^r G_{\mathbf{k}}(r,r') S_{\mathbf{k}}(r') r' \, dr' \tag{9}$$

where $S_{\mathbf{k}}(r')$ represents the source terms in the Poisson equation (4) located at r'. Note that (4-9) have been expressed in terms of the radial coordinate, r. However, unless otherwise stated, the discussion below is framed in terms of the wall-normal coordinate $y = (1-r)$ and velocity.

The magnitude of the Green's function at the wall ($y = 0$) corresponding to a source located at the wall ($y' = 0$) is shown in Fig. 1a. It is clear that the magnitude of the Green's function decreases with increasing streamwise and spanwise wavenumbers. Further, the contours are roughly symmetric in k and n. In agreement with prior observations, this suggests that for identical source strengths, *circular* structures with similar streamwise and spanwise length scales are likely to generate larger wall pressure signatures compared to structures elongated in either the streamwise or spanwise directions.

Figure 1b shows the variation in the Green's functions at the wall ($y = 0$) for varying source locations (y'), for four different wavenumber combinations: the triadically-consistent modes $\mathbf{k}_1 = (k,n) = (6,6)$, $\mathbf{k}_2 = (1,6)$, and $\mathbf{k}_3 = (7,12)$ considered by Sharma & McKeon (2013), along

with $\mathbf{k}_b = (60,60)$. The streamwise wavenumber k is normalized based on pipe radius, such that $k = 1$ corresponds to a streamwise wavelength $2\pi R$. The Green's functions corresponding to higher wavenumbers (e.g. $\mathbf{k}_b$, $\mathbf{k}_3$) decay very rapidly away from the wall compared to those for the lower wavenumbers (e.g. $\mathbf{k}_2$). As a result, larger-scale structures in the velocity field are likely to have a longer-range influence on wall pressure. At the same time, the source terms for the pressure Poisson equation (4) depend on gradients in the velocity fields. These gradients are likely to be smaller for the larger-scale structures.

Below, we consider the velocity and pressure fields for mode $\mathbf{k}_b$, as well as a packet comprising modes $\mathbf{k}_1$, $\mathbf{k}_2$, and $\mathbf{k}_3$. These fields are computed based on the singular value decomposition of the Navier-Stokes resolvent operator at Reynolds number $Re = 2\bar{U}R/\nu = 75 \times 10^3$ ($R^+ = 1800$), where $\bar{U}$ is the bulk-averaged mean velocity. The discretized resolvent operator in (2) is constructed using the experimental mean velocity data of McKeon *et al.* (2004).

SINGLE MODE

Figure 2 shows the velocity and pressure for the mode $\mathbf{k}_b = (k,n,\omega) = (60,60,30)$ computed under the singular value decomposition of the Navier-Stokes resolvent. This mode combination represents a helical wave of streamwise and spanwise wavelength $\lambda_x = \lambda_\theta = 2\pi R/60$ ($\lambda_x^+ = \lambda_\theta^+ \approx 190$), propagating downstream at half the pipe centerline velocity, $c = \omega/k = 0.5$ ($c^+ \approx 12$). The wall-normal location of the critical layer for this mode, where $U = c$, is $y_c^+ \approx 23$. Importantly, although we only consider a specific wavenumber-frequency combination, the results presented below are generally representative of the velocity and pressure fields predicted by the extended resolvent analysis.

Figure 2a shows that the magnitude of the streamwise velocity (u) peaks close to the critical layer. The wall-normal velocity (v) peaks at a location slightly further away from the wall, $y^+ \approx 30$. In general, the pressure magnitude (p) exhibits little variation ($< 20\%$) for $y^+ < 30$. However, there is a discernible peak in pressure near the critical layer $y^+ \approx 25$ (Fig. 2a), corresponding to the location where the rapid source term in the pressure Poisson equation (4) is maximum. The pressure decays for $y^+ > 40$, as the rapid source term becomes negligible.

Note also the distinct phase profiles for the velocity and pressure fields shown in Fig. 2b. The wall-normal velocity (fine black line) is approximately π out of phase with the streamwise velocity at the critical layer. Further, the phase of the streamwise velocity decreases by π across the critical layer (from $y^+ \approx 10$ to $y^+ \approx 40$). These phase profiles are typical of the critical layer solutions expected from linear analysis of the Orr-Sommerfeld-Squire equations. The π phase difference between the wall-normal and streamwise velocities comes about because the mean shear and viscous terms in the u-momentum equation must balance at the critical layer, $v_{\mathbf{k}} U' \sim \nabla_{\mathbf{k}}^2 u_{\mathbf{k}}$. When traveling downstream with the mode at speed c, this characteristic phase profile also leads to the well-known *cat's eye* streamline patterns in the streamwise-wall normal plane (see e.g. Fig. 3b). The cat's eye streamline pattern is associated with two-dimensional, inviscid Kelvin-Stuart vortices. Sharma & McKeon (2013) suggest that the response modes predicted by our model may be interpreted as the three-dimensional equivalent (regularized due to viscosity).

Fig. 2b shows that there is a nearly-constant $\pi/2$ phase difference between the pressure (gray line) and wall-normal

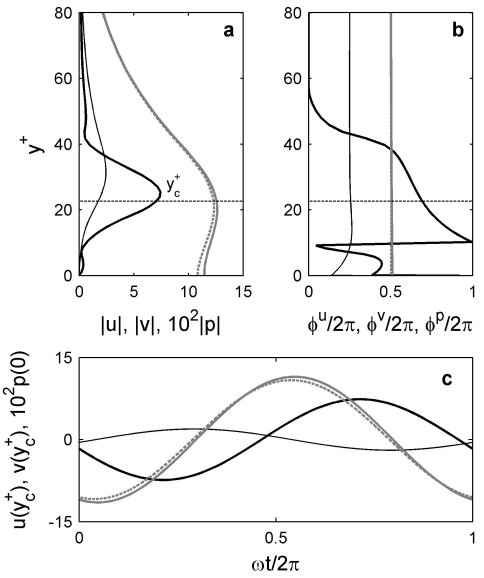

Figure 2: Wall-normal variation in the absolute magnitude (a) and phase (b) of the streamwise velocity (u, black line), wall-normal velocity (v, fine black line), and pressure (p, gray line) for the mode $\mathbf{k}_b = (60,60,30)$. (c) Temporal variation in wall pressure, and the streamwise and wall-normal velocities at the critical layer. Dashed gray lines represent the rapid component of pressure, computed using (9).

velocity field (fine black line). This means that the wall-normal velocity leads (lags) the pressure in space (time). Pressure minima occur during periods of rapidly increasing wall-normal velocity, as shown in Fig. 2c.

The constant $\pi/2$ phase difference between pressure and wall-normal velocity also suggests that the primary contribution to the pressure field comes from the rapid source term in the pressure Poisson equation (4) such that $\nabla_{\mathbf{k}}^2 p_{\mathbf{k}} \sim -ikv_{\mathbf{k}}U'$. This is further confirmed by the Green's function solutions to pressure shown in Fig. 2 (dashed gray lines). These solutions are computed based on (9), assuming contributions only from the rapid source term (i.e., $S_{\mathbf{k}} = -2ikv_{\mathbf{k}}U'$). There is close agreement between the Green's function solution and the pressure computed from the resolvent analysis, showing that the model developed here generates forcing mode shapes that are near solenoidal, $\nabla_{\mathbf{k}} \cdot \mathbf{f}_{\mathbf{k}} \approx 0$. Unlike McKeon & Sharma (2010), we do not enforce solenoidal $\mathbf{f}_{\mathbf{k}}$ in this paper. Solenoidal forcing arises naturally from the singular value decomposition as the input direction that leads to the largest velocity response (i.e., highest $\sigma_{\mathbf{k}}$). Intuitively, this may be attributed to the Helmholtz decomposition; non-solenoidal forcing does not directly contribute to the solenoidal velocity field, and hence the velocity response would be lower for such forcing (i.e., lower $\sigma_{\mathbf{k}}$). The dominance of the rapid pressure terms also underscores the link between the present model and the linear analysis associated with Rapid Distortion Theory (Hunt & Carruthers, 1990; Pope, 2000). This link will be elaborated elsewhere.

Sharma & McKeon (2013) show that structures resembling hairpin vortices arise from the superposition of two obliquely traveling modes. This is illustrated by the

swirling strength[1] isosurfaces shown in Fig. 3a for the superposed modes $\mathbf{k}_b^+ = (60,60,30)$ and $\mathbf{k}_b^- = (60,-60,30)$. The modes themselves generate an equal number of *prograde* and *retrograde* vortices. However, the presence of the shear associated with the mean velocity profile suppresses the retrograde vortices and strengthens the prograde vortices. The resulting structures appear consistent with prior observations (see Sharma & McKeon (2013) for more information). Note that the degree to which retrograde vortices are suppressed and prograde vortices are strengthened depends on the relative magnitude of the mean shear, and that associated with modes $\mathbf{k}_b^{\pm}$. Our model does not yield any information on the relative amplitudes of the mode and the mean velocity profile. The data shown in Fig. 3 assume that the amplitude of the mean velocity profile, U, is $100\times$ that of the modes $\mathbf{u}_{\mathbf{k}_b^+}$ and $\mathbf{u}_{\mathbf{k}_b^-}$.

A local pressure minimum is often used as an intuitive measure for vortex detection (Chakraborty *et al.*, 2005). The structures predicted by our model provide additional physical insight into this measure. Figure 3a shows that the heads of the hairpin vortices predicted by our model sit above wall pressure minima in the streamwise and spanwise directions. This is a direct consequence of the $\pi/2$ phase difference between wall-normal velocity and pressure shown in Fig. 2, whereby the minimum pressure coincides with periods of rapidly increasing wall-normal velocity (i.e., during periods of prograde rotation). In the wall-normal direction, the hairpin heads are located just above the critical layer (Fig. 3b). This is close to the location of the maximum pressure amplitude.

The boundary-layer experiments of Schewe (1983) and Johansson *et al.* (1987) showed that, despite their infrequent occurrence, periods of high intensity (i.e., large amplitude) wall pressure fluctuations contributed significantly to the long-time root-mean-square value for wall pressure. Conditional averages of the pressure measurements made by Johansson *et al.* (1987) at Reynolds number similar to that considered here ($\delta^+ = 1800$, where δ is boundary layer thickness) showed that these high amplitude pressure peaks originated from shear-layer structures in the buffer region of the flow, with characteristic length scale $L^+ \approx 150$ and advection speed $U_a^+ \approx 12$ (c.f. $\lambda_x^+ \approx 190, c^+ \approx 12$ for mode $\mathbf{k}_b$). Schewe (1983) obtained similar results at a lower Reynolds number ($\delta^+ \approx 600$). Johansson *et al.* (1987) also noted that large amplitude positive pressure peaks were associated with periods of increasing streamwise velocity and decreasing wall-normal velocity at $y^+ \approx 15$. The time-varying wall pressure and critical-layer velocities for mode $\mathbf{k}_b$, shown in Fig. 2c, reproduce all of these features. Further, Johansson *et al.* (1987) found that the amplitude of the pressure peak scaled linearly with the velocities measured at $y^+ \approx 15$, indicating the dominance of the linear, rapid component of pressure. In light of these observations, the high intensity pressure fluctuations observed by Schewe (1983) and Johansson *et al.* (1987) may be attributed to the presence of modes similar to $\mathbf{k}_b$ in the real flow.

THREE-MODE PACKET

Sharma & McKeon (2013) show that the triadically consistent combination of mode pairs $\mathbf{k}_1 = (6,\pm 6,4)$, $\mathbf{k}_2 = (1,\pm 6,2/3)$, and $\mathbf{k}_3 = (7,\pm 12,14/3)$, propagating at speed $c = 2/3$, can recreate realistic complex structure consisting of modulating hairpin vortex packets. Fig. 4 shows the swirl field associated with this mode combination. To arrive at these results, the complex amplitudes of the velocity and pressure fields for the three modes were set to $(a_1,a_2,a_3) = (1,4.5,0.83i)$ and the amplitude of the mean velocity profile was set to 1000, so that $\tilde{\mathbf{u}} = 1000\mathbf{u_0} + a_1\mathbf{u}_{\mathbf{k}_1^{\pm}} + a_2\mathbf{u}_{\mathbf{k}_2^{\pm}} + a_3\mathbf{u}_{\mathbf{k}_3^{\pm}}$. These amplitudes were selected to be representative of experiments. The swirl field for this mode combination shows packets of prograde, hairpin-like structures (Fig.4a). Together, the modes $\mathbf{k}_1$ and $\mathbf{k}_3$ would lead to a *beating* effect over a streamwise length scale $\approx 6R^+$, set by $\mathbf{k}_1 - \mathbf{k}_3$. The additional longer $\mathbf{k}_2$ mode organizes the hairpins into discrete packets with the same streamwise length scale.

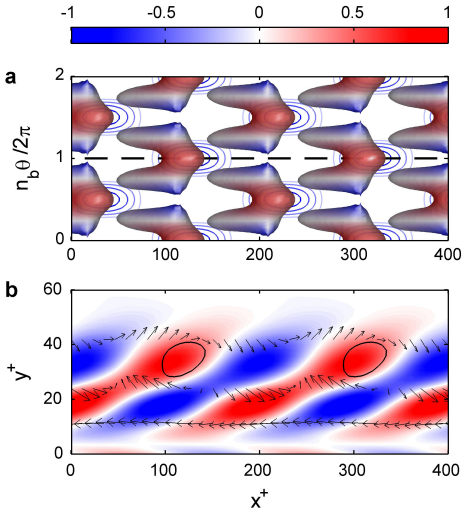

Figure 3: (a) Swirling strength isosurfaces (at 50% of maximum) for the superposed modes $\mathbf{k}_b^+$ and $\mathbf{k}_b^-$. The isosurfaces are colored based on the local azimuthal vorticity; red denotes *prograde* rotation (i.e., in the direction of mean shear) and blue denotes *retrograde* rotation. The contours beneath the isosurfaces show the normalized wall pressure field (contours at -0.8,-0.6,-0.4,-0.2). (b) Azimuthal vorticity at the spanwise location $n\theta/2\pi = 1$ (dashed line in a). Solid lines show swirling strength isocontours at 50% of maximum value. Arrows show the velocity relative to the propagation speed of the mode, $c = 0.5$ (not to scale).

Figure 4 shows that the hairpin-like structures are associated with wall pressure minima. As before, this can be attributed to the $\pi/2$ phase difference between the wall-normal velocity and pressure (Fig. 2b). The wall pressure field is dominated by structures corresponding to mode $\mathbf{k}_1$ (i.e., with streamwise and spanwise length scale $L^+ \approx R^+ = 1800$) despite the amplitude of mode $\mathbf{k}_2$ being set to $4.5\times$ that for mode $\mathbf{k}_1$. The larger wall pressure for mode $\mathbf{k}_1$ is explained by the form of the rapid source term in the pressure Poisson equation, $S_{\mathbf{k}} \sim kv_{\mathbf{k}}U'$ (4). Since $k_1 = 6k_2$ and $|v_{\mathbf{k}_1}|_{max} \approx 4|v_{\mathbf{k}_2}|_{max}$, the source term is $\approx 24\times$ larger for mode $\mathbf{k}_1$ compared to mode $\mathbf{k}_2$. This increase in source strength leads to a 16-fold increase in wall pressure for the smaller $\mathbf{k}_1$ mode, which offsets the higher amplitude of mode $\mathbf{k}_2$. In contrast to the wall pressure, the magnitude of the streamwise velocity is comparable for all three modes. As a result, the longer $\mathbf{k}_2$ mode dominates the streamwise velocity field given its higher amplitude, $a_2 = 4.5$ (data not shown). These results are broadly consistent with the DNS of Jimenez & Hoyas (2008), who show that the streamwise

[1]The imaginary component of the complex conjugate eigenvalue of the velocity gradient tensor (Chakraborty *et al.*, 2005)

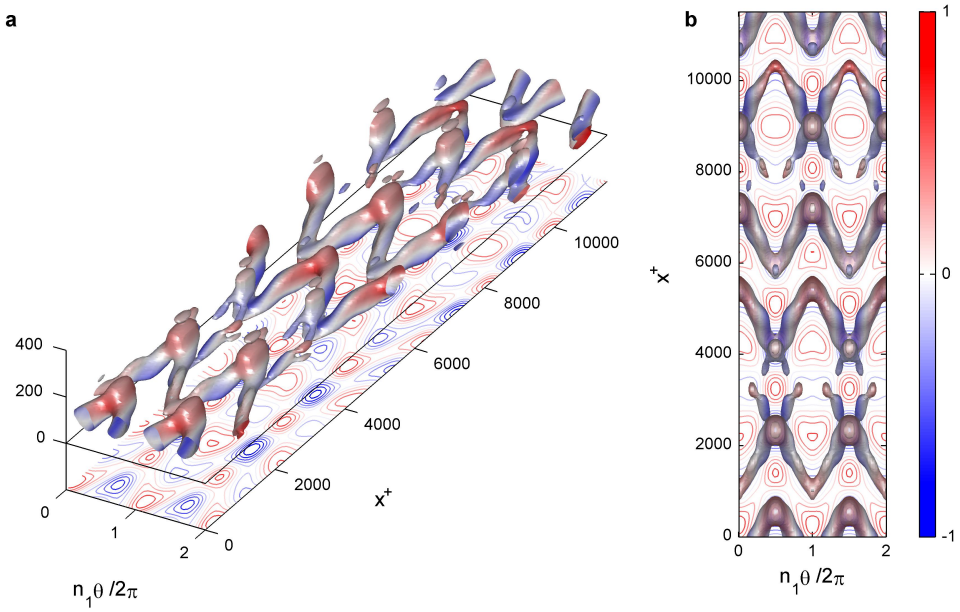

Figure 4: (a) Isometric and (b) plan views of swirling strength isosurfaces (at 50% of maximum) for the modulating packet comprising modes $\mathbf{k}_1$, $\mathbf{k}_2$ and $\mathbf{k}_3$. The isosurfaces are shaded based on the local azimuthal vorticity; red denotes *prograde* rotation and blue denotes *retrograde* rotation. The contours beneath the isosurfaces show the wall pressure field. Red (blue) contour lines denote regions of high (low) pressure.

length scales associated with the pressure spectrum tend to be smaller than those associated with the streamwise velocity spectrum.

Finally, although we only consider a single wave speed, c, in this section, the form of the Green's function solution permits further comment. The model developed here predicts that wall turbulence is dominated by mode shapes resembling critical-layer solutions. Hence, we anticipate that modes with lower c are likely to be localized closer to the wall, in regions of higher mean shear (U'), leading to an increase in the strength of the rapid source term in the pressure Poisson equation (4). Everything else being equal, this increase in source strength coupled with the closer proximity to the wall, is likely to result in larger wall pressure fluctuations for modes with lower c.

ACKNOWLEDGMENTS

The authors acknowledge financial support from the Air Force Office of Scientific Research grant FA9550-12-1-0469, Program Manager Doug Smith (ML, BJM).

REFERENCES

Chakraborty, P., Balachandar, S. & Adrian, R. J. 2005 On the relationships between local vortex identification schemes. *Journal of Fluid Mechanics* **535**, 189–214.

Hunt, J. C. R. & Carruthers, D. J. 1990 Rapid distortion theory and the 'problems' of turbulence. *Journal of Fluid Mechanics* **212**, 497–532.

Jimenez, Javier & Hoyas, Sergio 2008 Turbulent fluctuations above the buffer layer of wall-bounded flows. *Journal of Fluid Mechanics* **611**, 215–236.

Johansson, A. V., Her, J. Y. & Haritonidis, J. H. 1987 On the generation of high-amplitude wall-pressure peaks in turbulent boundary-layers and spots. *Journal of Fluid Mechanics* **175**, 119–142.

Kim, J. 1989 On the structure of pressure-fluctuations in simulated turbulent channel flow. *Journal of Fluid Mechanics* **205**, 421–451.

Kim, J. 2003 Control of turbulent boundary layers. *Physics of Fluids* **15** (5), 1093–1105.

Klewicki, J., Priyadarshana, P. J. A. & Metzger, M. M. 2008 Statistical structure of the fluctuating wall pressure and its in-plane gradients at high Reynolds number. *Journal of Fluid Mechanics* **609**, 195–220.

Koumoutsakos, P. 1999 Vorticity flux control for a turbulent channel flow. *Physics of Fluids* **11**, 248.

McKeon, B. J., Li, J., Jiang, W., Morrison, J. F. & Smits, A. J. 2004 Further observations on the mean velocity distribution in fully developed pipe flow. *Journal of Fluid Mechanics* **501**, 135–147.

McKeon, B. J. & Sharma, A. S. 2010 A critical-layer framework for turbulent pipe flow. *Journal of Fluid Mechanics* **658**, 336–382.

Moarref, R., Sharma, A. S., Tropp, J. A. & McKeon, B. J. 2013 Model-based scaling and prediction of the streamwise energy intensity in high-Reynolds number turbulent channels. ArXiv:1302.1594 [physics.flu-dyn].

Pope, Stephen B. 2000 *Turbulent Flows*. Cambridge University Press, UK.

Schewe, G. 1983 On the structure and resolution of wall-pressure fluctuations associated with turbulent boundary-layer flow. *Journal of Fluid Mechanics* **134**, 311–328.

Sharma, A. S. & McKeon, B. J. 2013 On coherent structure in wall turbulence. ArXiv:1301.7580v1 [physics.flu-dyn].

Tsuji, Y., Fransson, J. H. M., Alfredsson, P. H. & Johansson, A. V. 2007 Pressure statistics and their scaling in high-Reynolds-number turbulent boundary layers. *Journal of Fluid Mechanics* **585**, 1–40.

Tsuji, Y., Imayama, S., P., Schlatter, Alfredsson, P. H., Johansson, A. V., Marusic, I., Hutchins, N. & Monty, J. 2012 Pressure fluctuation in high-Reynolds-number turbulent boundary layer: results from experiments and dns. *Journal of Turbulence* **13** (50), 1–19.